

3-Dimensional Model Based Iterative Reconstruction of Magnetisation in a Nanowire Structure Using Holographic Vector Field Electron Tomography Measurements

Aurys Šilinga^{1,*}, András Kovács², Stephen McVitie¹,
Rafal E. Dunin-Borkowski², Kayla Fallon¹ and Trevor P. Almeida^{1,*}

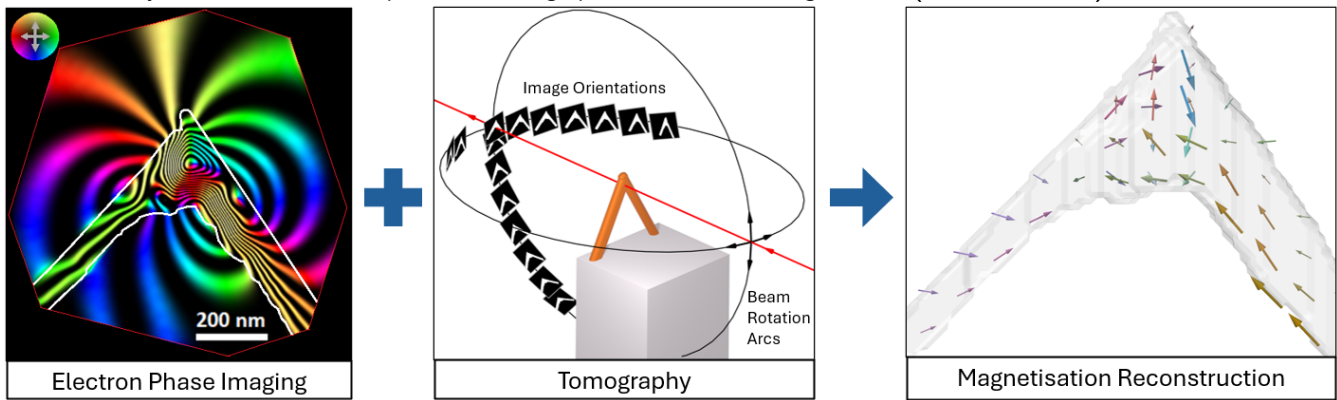
¹School of Physics and Astronomy, University of Glasgow, Kelvin Building, G12 8QQ, Scotland, United Kingdom and ²Ernst Ruska-Centre for Microscopy and Spectroscopy with Electrons, Forschungszentrum Jülich GmbH, Wilhelm-Johnen-Straße, 52428 Jülich, North Rhine-Westphalia, Germany

*Corresponding authors: a.silinga.1@research.gla.ac.uk, trevor.almeida@glasgow.ac.uk

FOR PUBLISHER ONLY Received on Date Month Year; revised on Date Month Year; accepted on Date Month Year

Abstract

Methods for characterisation of 3D magnetic spin structures are necessary to advance the performance of 3D magnetic nanoscale technologies. However, as the component dimensions approach the nanometre range, it becomes more challenging to analyse 3D magnetic configurations with the appropriate spatial resolution. In this paper, we present a method based on Lorentz transmission electron microscopy in which model-based iterative reconstruction (MBIR) is used to reconstruct the most probable magnetisation in an exemplar nanostructure. This method is based on relating electron phase measurements to the magnetic configuration of the nanostructure, and therefore, the method is subject to certain limitations. In this proof-of-concept experiment, MBIR was tested on an L-shaped ferromagnetic cobalt nanowire, fabricated using focused electron beam induced deposition. Off-axis electron holography was used to acquire a tomographic tilt series of electron holograms, which were analysed to measure magnetic electron phase shift over two tilt arcs with up to $\pm 60^\circ$ tilt range. Then, a 3D magnetisation vector field consistent with the tomographic phase measurements was reconstructed, revealing multiple magnetic domains within the nanowire. The reconstructed magnetisation is accurate for magnetic domains larger than 50 nm, and higher resolution can be achieved by the continued development of tomographic reconstruction algorithms. (Max 200 words)



Key words: Lorentz TEM, 3D imaging, tomography, magnetism, magnetic materials, FEBID, MBIR

Introduction

Introduction to 3D magnetic characterisation

Due to advancements in characterisation, fabrication, and discovery of more complex spin textures such as skyrmions and hopfions [Zheng et al., 2023], there has been a drive to explore the properties of three-dimensional (3D) magnetic configurations for a range of applications including spintronics. Spintronic circuits comprised of integrated magnetic nanowires have been proposed for next-generation data storage applications [Parkin et al., 2008] and as physical components for improving machine-learning efficiency [Ellis et al., 2023]. Spintronic computing is being developed due to its fundamentally higher energy efficiency data storage compared to capacitor-based electronics [Nikonov et al., 2006], but most prototypes so far have been fabricated using two-dimensional (2D) lithographic techniques, and the 3D stacking needed for commercial implementation has not been realised. For example, magnetic racetrack memory (RM) prototypes have demonstrated storage and manipulation of data that is carried by magnetic domains in flat patterned nanowires, but expanding into 3D nanowire architectures would markedly increase the storage density per unit area [Gu et al., 2022]. As prototypes of 3D architectures are developed, experimental measurements of magnetic structure and domain movement in 3D can guide further development of RM-type technologies. The observables used to characterise ferromagnetic samples are related by

$$\vec{B} = \mu_0(\vec{H}(\vec{M}) + \vec{M}) \quad (1)$$

where \vec{M} is the magnetisation vector field describing magnetic moment per unit volume, \vec{B} is the magnetic induction, and μ_0 is the vacuum permeability. If no external magnetic fields, conduction currents, or displacement currents are present, \vec{H} is the demagnetising field defined by the distribution of \vec{M} . Nanoscale measurements of \vec{M} are necessary to characterise magnetic 3D nanostructures, and X-ray imaging allows 3D reconstruction of \vec{M} with 50 nm resolution using magnetic laminography [Donnelly et al., 2020] or 70 nm with Fourier transform holography [Donnelly et al., 2017, Di Pietro Martínez et al., 2023]. It should be noted that theoretical predictions estimate X-ray laminography resolution up to 20 nm [Donnelly et al., 2022]. In comparison, transmission electron microscopy (TEM) cannot uniquely reconstruct \vec{M} , but has been used to measure \vec{B} with a higher 3D resolution of 10 nm using the TEM technique of holographic vector-field electron tomography (H-VFET) [Phatak et al., 2008, 2010, Wolf et al., 2019]. In TEM, micromagnetic simulations are conventionally used to aid the interpretation of \vec{B} measurements [Donahue and McMichael, 1997, Lyu et al., 2024]. This work presents an alternative to simulations by applying MBIR to reconstruct a distribution of \vec{M} consistent with measured \vec{B} . This paper discusses how electron phase measurements are used to combine magnetic and electrostatic signals to improve \vec{M} reconstruction accuracy, what experimental limitations have been considered, and in which cases MBIR can achieve better resolution than X-ray imaging methods.

Scope of \vec{M} reconstruction with MBIR

MBIR has been applied to develop a tomographic reconstruction method for interpreting \vec{M} from H-VFET datasets, without requiring prior knowledge of the sample [Caron, 2018a]. The most common magnetic imaging techniques in the TEM [Lubk and

Zweck, 2015, Kohn et al., 2016, Krajnak et al., 2016, You et al., 2023, Cui et al., 2024], collectively known as Lorentz microscopy, fundamentally rely on an interpretation of the Aharonov-Bohm effect [Aharonov and Bohm, 1959] that describes how the phase of an electron wave is affected by electromagnetic potentials. The interaction of electron waves travelling through a magnetic induction field \vec{B} introduces a corresponding electron phase shift φ_{mag} , such that

$$\int \vec{B} \times d\vec{z} = \frac{\hbar}{e} \vec{\nabla} \varphi_{mag} \quad (2)$$

where e is the electron charge, \hbar is the reduced Planck constant, $d\vec{z}$ is a path element along the electron beam, and the phase gradient $\vec{\nabla} \varphi_{mag}$ is defined in the 2D plane perpendicular to the electron beam. In general, Lorentz microscopy can be used to recover the φ_{mag} , therefore MBIR is applicable to all Lorentz TEM techniques. The recovery of φ_{mag} from electron holograms for this experiment is described in the methods section. In many cases, there will be \vec{H} fields present such that \vec{B} and \vec{M} are not equivalent. However, for the imaging conditions where \vec{H} results only from the \vec{M} configuration, the magnetic phase effects are considered to arise from the $\text{curl}(\vec{M})$ component parallel to the electron beam [McVitie and White, 2003]. This $\text{curl}(\vec{M})$, an Amperian current, is the source of the \vec{B} which contributes to the electron phase and is associated only with the sample. Under the above conditions the \vec{M} of vortex domain walls (DWs) has been measured [Junginger et al., 2008] but required tomography to evaluate all the components of $\text{curl}(\vec{M})$. Overall, the reconstruction error depends on the type of sample, angular imaging range, and correction of TEM instrument misalignments. However, if a nanostructure can be incrementally tilted to high angles and φ_{mag} is detected from all parts of the sample, then all the information needed for reconstruction can be extracted from the phase measurements. Simulation-based error estimates for this experiment are discussed in the methods section and the supplementary material [S1].

The workflow for the reconstruction of \vec{M} (Fig. 1) consists of: 1) processing and alignment of the experimental data to construct a model of the sample; 2) MBIR reconstruction of a possible \vec{M} distribution that best matches the experimental data; and 3) optimal estimation diagnostics for evaluating reconstruction errors. A method that can compute rigorous estimates of 3D \vec{M} from experimental data has previously been theorised, and some parts of the software, such as a numerical solver [Mohan et al., 2018] and automated alignment [Houben and Bar Sadan, 2011], have been proposed separately. The theory of applying MBIR for \vec{M} reconstruction has been developed and extensively tested using simulated datasets [Caron, 2018b]. This work is an experimental development, showing the correction of errors caused by electron beam alignment [Diehle et al., 2021], sample drift, beam rotation, and surface damage present in experimental data.

Null spaces in electron phase measurement

Some configurations of \vec{M} are invisible to TEM [Mansuripur, 1991], and MBIR reconstructions of configurations that contribute no signal results in null spaces, that is volumes where the reconstructed \vec{M} is falsely close to zero [Caron, 2018c]. In simple terms, null spaces can exist due to projections where \vec{M} vector components sum to zero or having non-zero divergence of \vec{M} . In the case of unfavourable projections, tilting the sample is enough to reveal the hidden components, whereas divergent components can

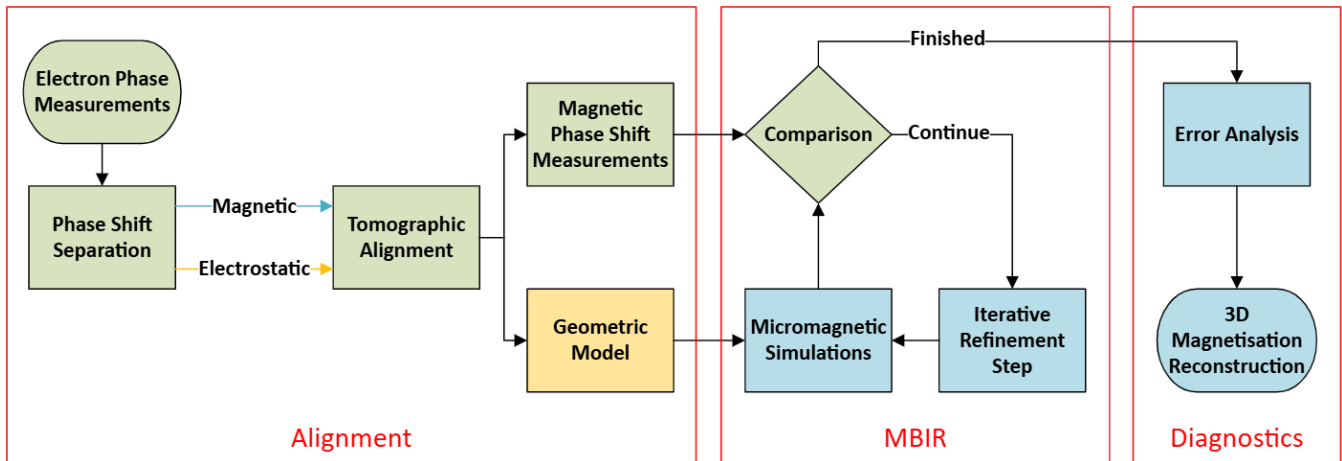


Fig. 1: Workflow for the reconstruction of 3D \vec{M} . The red boxes indicate the major processing steps: alignment, reconstruction with MBIR, and diagnostics. The steps are shaded to indicate what data type is being processed: 2D phase images (green), 3D magnetic vector fields (blue), or 3D electrostatic scalar fields (yellow). H-VFET datasets are processed to acquire both, a geometric mask defining where the magnetic material is located, and a series of magnetic phase shift measurements corresponding to \vec{B} field projections. Micromagnetic simulations are then performed at every iterative step to generate distributions of \vec{M} until a distribution is found that best matches the measured phase shifts. Finally, optimal estimation diagnostics are performed to evaluate random and systematic errors present in the reconstruction. Alignment of experimental datasets improves reconstruction accuracy and diagnostics evaluate the precision.

be problematic where even tilting may still result in contributions to the phase measurement remaining undetectable. Therefore, some configurations of \vec{M} , such as Neél domain walls, cannot be fully reconstructed. How the MBIR algorithm assigns null values to \vec{M} states that do not contribute signal, and examples of such states, are discussed in the supplementary material [S2]. It should be noted that null spaces are not present in the experimental reconstruction described in this paper.

Materials and Methods

Sample fabrication and characterisation

An L-shaped intersection between ferromagnetic cobalt nanowires was chosen to test the 3D reconstruction algorithm, as this corresponds to an element of a 3D racetrack-memory configuration, and these structural features can act as DW pinning sites. To perform TEM imaging of the magnetic states arising at such geometric DW pinning sites, free-standing cobalt nanowires were fabricated on a copper substrate using FEBID, in a process akin to nanoscale 3D printing in a scanning electron microscope (SEM) [Skoric et al., 2020, Magén et al., 2021]. As shown in Fig. 2, a precursor gas is injected into the SEM chamber and cobalt is deposited at locations where the electron beam interacts with the sample. The geometry of the deposited structure is controlled by translating the beam in a controlled manner using the SEM scan coils. The structure in Fig. 3a, consisting of two intersecting nanowires, was fabricated by modelling the deposition for a geometry defined with computer-assisted design (CAD) [Skoric et al., 2020] and depositing by electron irradiation of $\text{Co}_2(\text{CO})_8$ precursor in an FEI HELIOS Plasma FIB and SEM. The deposition was performed using a 30 kV electron beam with 690 pA beam current, and $6 \cdot 10^{-5}$ Pa chamber deposition pressure. The dimensions and morphology of the sample were obtained by imaging the intersection from multiple tilt angles in the SEM,

such as the top-down image Fig. 3b. Scanning TEM electron energy loss spectroscopy (STEM EELS) was employed for chemical analysis of the green and red boxed regions areas in Fig. 3a to obtain an elemental map (Fig. 3d) and cross-sectional line profile (Fig. 3e), respectively. The chemical analysis shows that the nanowires were deposited such that the nanowire core has cobalt purity in the range of 45% to 60%, and the surface is covered in a shell of amorphous carbon and oxygen. The radial dependence of cobalt content in the cross-sectional elemental map in Fig. 3e suggests that the deposition was performed in the beam-limited FEBID regime [Serrano-Ramón et al., 2011], where the material that received the highest radiation dose during deposition obtained the highest purity. The Lorentz TEM technique of off-axis electron holography was performed to image the local magnetic configuration of nanowires and is discussed in detail later. Prior to tomographic imaging, the sample was magnetically saturated by applying a 1 T magnetic field in the plane of the nanowire perpendicular to the substrate and relaxed into the magnetic state shown in Fig. 3c. The magnetic phase image relates to a projection of \vec{B} by eq. 2 and shows projected \vec{B} direction and relative magnitude. The measured phase shift is affected by variations in cobalt purity, projected sample thickness, and orientations of $\text{curl}(\vec{M})$. Furthermore, the sample has a head-to-head magnetic DW with a vortex configuration, therefore, tomographic imaging is needed for full magnetic characterisation.

Holographic vector-field electron tomography

In this work, off-axis electron holography [Dunin-Borkowski et al., 2019] is performed as the preferred Lorentz microscopy method because it measures electron phase shift directly and is suitable for tomography, as it has high phase sensitivity corresponding to 0.016 rad root-mean-square noise, 10 second exposure time per phase image, and causes minimal sample damage with a low electron flux of $200 \text{ e/nm}^2/\text{s}$. All electron holography tilt-series for H-VFET

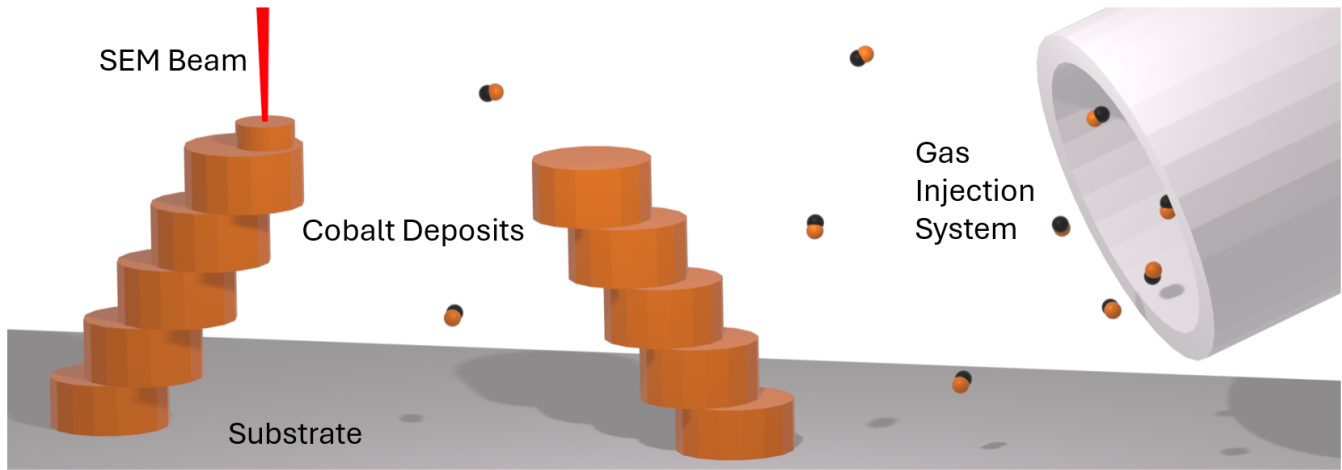


Fig. 2: FEBID fabrication model. Cobalt is deposited locally where the electron beam interacts with solid material. The beam is translated to effectively control the location of each deposit.

were acquired using the FEI Titan G2 60-300 HOLO, at 300kV. For this study, a voltage of 100 V was applied to the biprism and resulted in electron holograms (Fig. 4a) with interference fringe spacing of ~ 3.1 nm, as shown in Fig. 4a left inset. The electron wave phase, Fig. 4b, was calculated from the inverse fast Fourier transform (FFT) of the sideband in Fig. 4a right inset [Mitchell and Schaffer, 2005, Boureau et al., 2018, Dunin-Borkowski et al., 2019]. At each position, five holograms with individual exposure times of 2 s were acquired and their calculated phase images were averaged to reduce the effects of time-dependent fluctuations. A large TEM pole-piece gap (~ 11 mm) and a dedicated tomography holder [Diehle et al., 2021] allow samples to be tilted 360° around the holder axis without removing them from the microscope.

For the tomographic reconstruction, electron holograms were acquired at 10° tilt intervals over two arcs, but the effective maximum tilt angles were limited from -60° to 30° and -60° to 0° as the sample was eclipsed by the sample holder and the substrate. The second tilt series arc was acquired to reduce missing wedge artefacts and prevent projection-based null spaces [Caron, 2018c]. Simulations of samples comprising uniformly magnetised nanowires and vortex configurations have shown that imaging at smaller intervals has a negligible impact on reconstruction quality [Caron, 2018b]. Furthermore, if the available imaging range is used, and a 10% difference between the volumes of the sample and its geometric model is assumed; then the difference between the \vec{M} reconstruction and the ground truth is on average less than 10% per voxel, which was evaluated by simulations discussed in the supplementary material [S1]. To separate the electrostatic and magnetic contributions to the phase images, electron holograms were acquired before and after tilting the sample by 180° to change the sign of the magnetic phase contribution. According to the expression for the phase of an electron passing vertically through a sample [Aharonov and Bohm, 1959, Weyland and Midgley, 2016],

$$\begin{aligned} \varphi(x, y) &= \varphi_{el}(V) + \varphi_{mag}(\vec{A}) = \\ &= \frac{e}{\hbar\nu} \int V(x, y, z) dz + \frac{e}{\hbar} \int \vec{A}(x, y, z) \cdot d\vec{z}, \end{aligned} \quad (3)$$

the contribution of magnetic vector potential changes sign when the beam direction \vec{z} is rotated 180° relative to the sample. In

eq. 3, $\varphi_{el}(V)$ and $\varphi_{mag}(\vec{A})$ are the phase shift contributions from the electrostatic and magnetic potential respectively, ν is the relativistic electron speed, and dz and $d\vec{z}$ are the respective scalar and vector elements of the electron path. For a pair of mutually upside-down holograms, the half-sum and half-difference of the measured phase images represent φ_{el} and φ_{mag} contributions to the phase shift respectively. Physically flipping the sample by 180° introduces misalignments between the hologram pair and the correction was automated with Python by identifying matching features on the sample edges [Walt et al., 2014, Peña et al., 2019, Paterson et al., 2020]. The necessary algorithms are listed in the supplementary material [S3]. To correct linear distortions caused by the alignment of the electron optical system of the TEM, an affine transformation is calculated to provide the optimal match between the edges of each phase image pair, as illustrated in Fig. 4c. In this experiment, the images are found to be elongated by 2% along the direction that forms a 75° angle with the tilt axis, which corresponds to constant non-uniformity of magnification that was measured by tilting a calibration sample by 180° and tracking fiducial markers. This introduces errors in distance measurements that are not corrected, but automated alignment corrects the resulting artefacts arising during phase separation. By applying the affine transformation, the phase separation artefacts are reduced below the noise level, such that they are not detectable in line profiles, ensuring consistent separation of φ_{el} and φ_{mag} , as in Fig. 4b (inset).

Alignment of phase images

The pairs of phase shift images are further processed before tomographic reconstruction. The φ_{mag} image can include pixels where the hologram-to-phase calculation is discontinuous, and therefore a confidence mask is defined to identify parts of the phase image that are valid for the reconstruction. The φ_{el} image is first flattened to remove background ramps induced by charging from the adjacent environment and the perturbed hologram reference. A threshold is then applied to define a mask that identifies where the material is located at each tilt angle. If elemental mapping was performed like in Fig. 3e, the threshold can be fine-tuned to

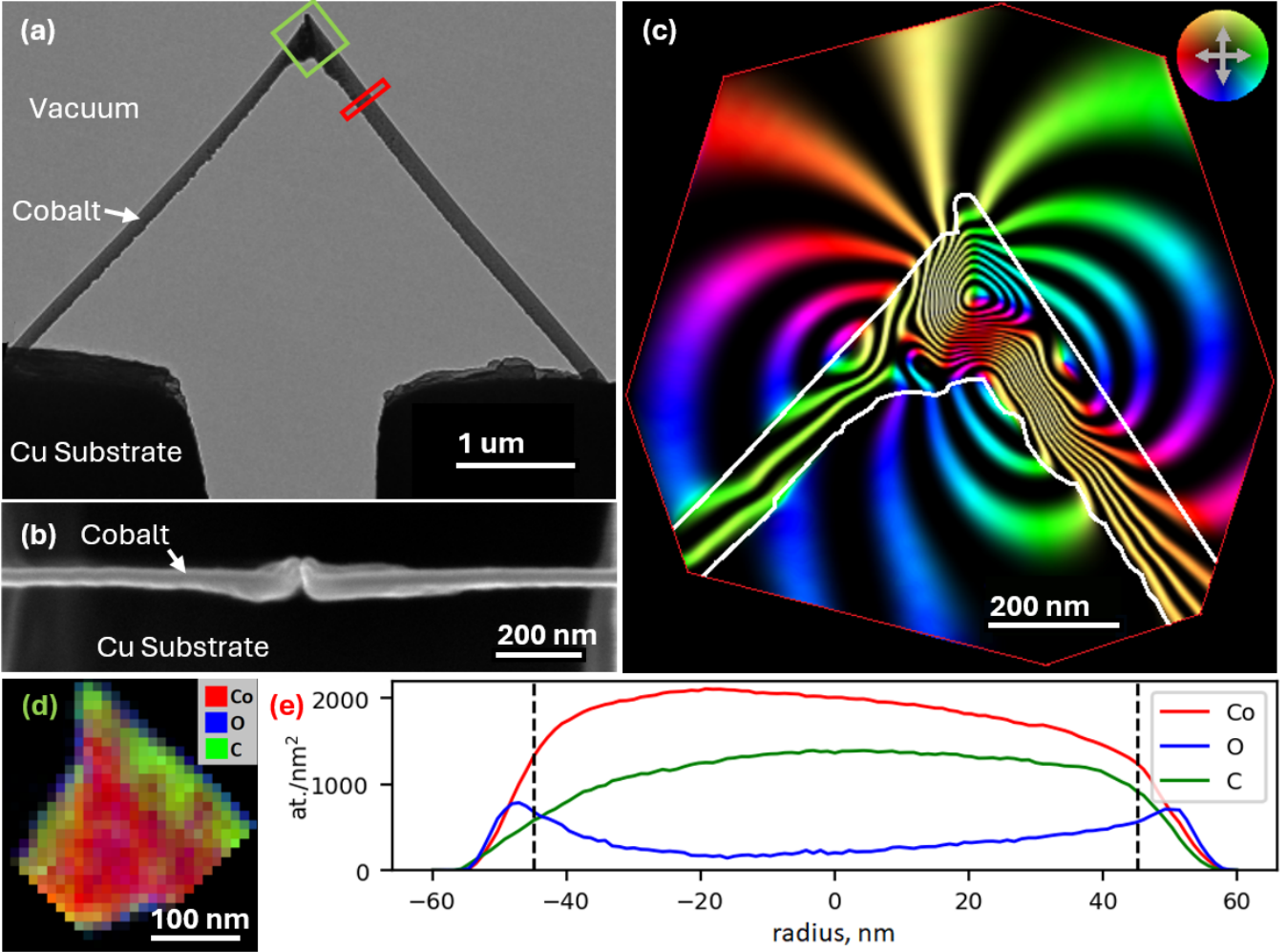


Fig. 3: Dimensions, morphology, and chemical analysis of the cobalt nanostructure fabricated with FEBID. (a) Bright-field (BF) TEM side-view image of the sample, showing areas which correspond to the elemental map (green box) and cross-sectional line profile (red box) shown in (d) and (e) respectively. (b) SEM image of the top-down view of the sample tip. (c) Magnetic phase contour image from electron holography, calculated as $\cos(6\varphi_{mag})$, with 1 rad line spacing, coloured to show the direction of the projected \vec{B} field (inset), and showing sample outline. (d) EELS chemical map of the tip showing the elemental distribution of Co, O and C. (e) Cross-sectional EELS elemental line profile showing that the central 90 nm of the nanowire has a cobalt content in the range 45% – 60%. The nanostructure is L-shaped, magnetic, and consists primarily of cobalt.

only include magnetic material in the mask. The binary magnetic material masks are the main images used for the alignment of the tilt series. Since the phase images have a spatial resolution of less than 6 nm due to hologram fringe spacing, the tomographic reconstruction is highly sensitive to misalignments. Sample drift is detected in all images, and the sample orientation is not known precisely during acquisition as only the relative tilt between two phase images, $\Delta\theta_i$, is measured. Therefore, the projection positions shown in Fig. 5a are refined using an axial-symmetry-based implementation of the common lines method [Penczek et al., 1996]. As illustrated in Fig. 5b, for every sample tilt $\Delta\theta_i$ there is a unique projection orientation α_i , and the two are related via the geometric parameters: ϕ is the observed detector rotation relative to the sample tilt-axis; θ_0 is the starting tilt of the sample; and α_0 is the sample orientation at 0° tilt. α_i can be measured by

finding the sample symmetry axis in the electrostatic phase maps, as shown in Fig. 5c. Then the equation

$$\tan(\alpha_i + \phi) = \tan(\alpha_0 + \phi) \cos(\theta_0 + \Delta\theta_i) \quad (4)$$

is true for all projections and can be solved to find unknown constants $(\alpha_0, \phi, \theta_0)$ defining absolute sample orientation. For a single tilt-series $i \in [1, \dots, n]$, and if the number of projections $n > 3$, the system of equations is over-defined and is numerically solved by multivariate minimisation [Virtanen et al., 2020]. Once aligned, the electrostatic phase images are back-projected to compute a scalar computed tomography (CT) reconstruction, shown in Fig. 5d, that defines the geometry of the sample. To correct missing wedge artefacts, the geometric model (Fig. 5d) is cropped to match the sample dimensions observed in SEM images (Fig. 3b). The refined model is used in the \vec{M} reconstruction to define where the magnetic material is located. It should be noted that the alignment

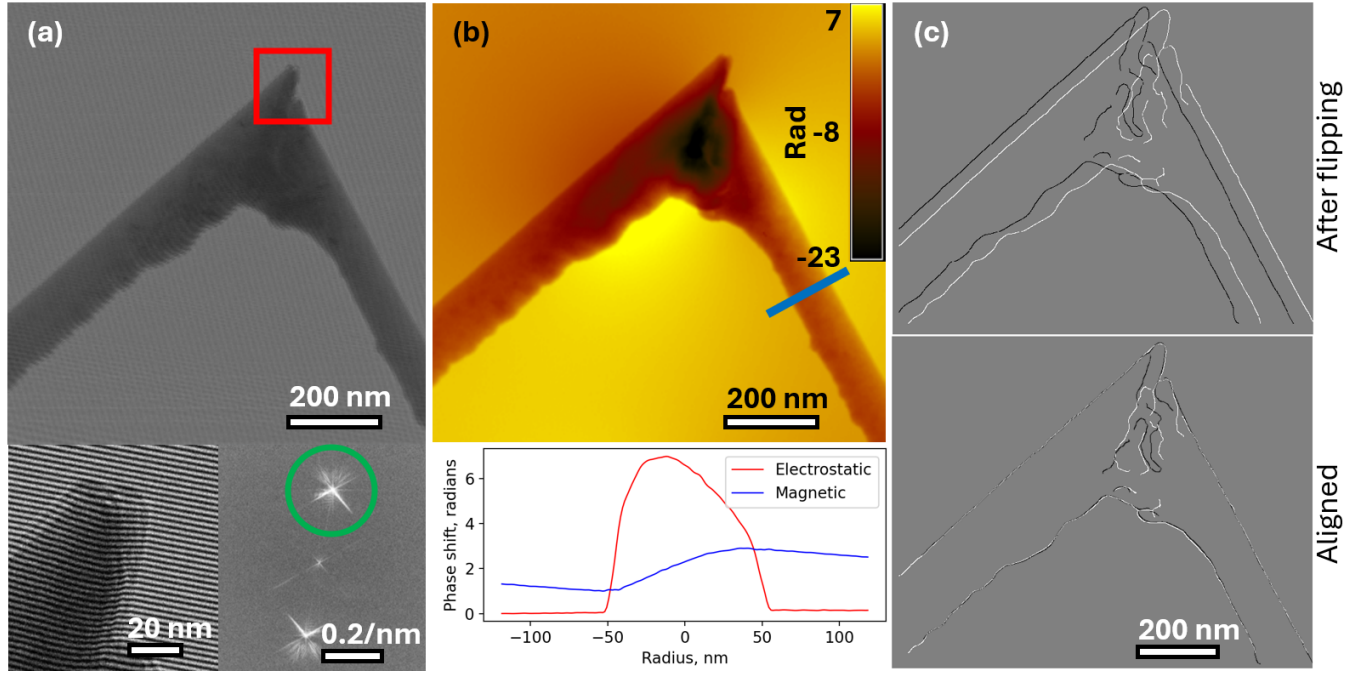


Fig. 4: Electron holograms and alignment of calculated phase images. (a) Electron hologram formed by interference of two electron waves. Insets show the magnified image inside the red box (bottom left) and the FFT (bottom right). The green circle in the FFT indicates the sideband used to calculate (b). (b) Total phase image obtained by analysing the hologram in reciprocal space. The inset shows the line profile of phase shift contributions along the blue line. (c) Alignment of phase images. To isolate the magnetic phase contribution the sample is flipped by 180°. This introduces distortions resulting in sample edge misalignment (top) that is corrected (bottom) by applying an affine transformation.

algorithm is imperfect, therefore blurring of features is observed and the 3D spatial resolution of the CT reconstruction is lower than the 6 nm 2D resolution of the phase images. Due to these misalignments, the reconstruction uses a 10.2 nm voxel size as using smaller voxel sizes did not improve the \vec{M} reconstruction resolution, which is discussed in detail in the diagnostics section.

3D \vec{M} reconstruction

To compute the 3D \vec{M} distribution, a forward model is defined that can simulate a tilt series of magnetic phase images for any \vec{M} contained within the geometric 3D model Fig. 5d [Caron, 2018d]. In order to determine a \vec{M} that would simultaneously satisfy all magnetic phase measurements, a cost function that is minimal for a \vec{M} that yields the closest fit is defined as

$$C = \sum_i (\varphi_{i,meas} - \varphi_{i,sim}(\vec{M}))^2 + \lambda_1 \sum_j (\vec{\nabla} M_j \cdot \vec{\nabla} M_j) + \lambda_2 \text{var}(|\vec{M}|) \quad (5)$$

where C is the cost to minimise, M_j are the magnetisation vector field components, φ_i are the phase image pixels, λ are the regulariser weights, $\vec{\nabla}$ is the gradient operator, and "var" is the variance operator. To account for multiple equivalent solutions, regularising terms are added to break the degeneracy by favouring a solution that exhibits low gradients and low variance in \vec{M} magnitude. The low gradients were chosen to favour ferromagnetic solutions and the low variance favours solutions comprising similar

materials. The cost function is minimised using a conjugate gradient method [Nocedal and Wright, 2006] and is initialised with $\vec{M} = 0$. The regulariser weights, λ in eq. 5, can be varied over 3 orders of magnitude and the reconstruction retains the same features, confirming that the solution is measurement-based. The reconstructed 3D distribution \vec{M}_{rec} is obtained using $\lambda_1 = 1$, which is the minimum value needed to lift the degeneracy between ferromagnetic and ferrimagnetic ordering, and $\lambda_2 = 0.1$ reduces surface artefacts without affecting the rest of the reconstruction.

Fig. 6a shows that there are multiple magnetic domains and the magnitude of \vec{M}_{rec} is highest at the bottom part of the intersection (denoted by the length of the arrows), in agreement with the radial cobalt distribution from Fig. 3e. To view domain walls inside the structure, the angles between pairs of neighbouring vectors are computed and the maximum angle is projected in Fig. 6b. The spin angle of $\sim 90^\circ$ identifies the core of vortex DW, and the dashed blue line shows the core direction, which corresponds to $\text{curl}(\vec{M}_{rec})$ direction at sub-volumes around the vortex core. The vortex state occupies the full $\sim 200 \text{ nm} \times 200 \text{ nm} \times 100 \text{ nm}$ volume of the nanowire intersection, and the U-shaped vortex core is 350 nm long. Fig. 6c-d display z-slices through \vec{M}_{rec} shown at full resolution and marking intersections with the vortex DW.

Diagnostics of the reconstruction

Reconstruction noise is assessed by Fourier shell correlation, by halving the 3D \vec{M}_{rec} dataset through random sampling and interpolating the missing values. Fig. 7 displays an estimate of signal-to-noise ratio (SNR) per spatial frequency band in the 3D

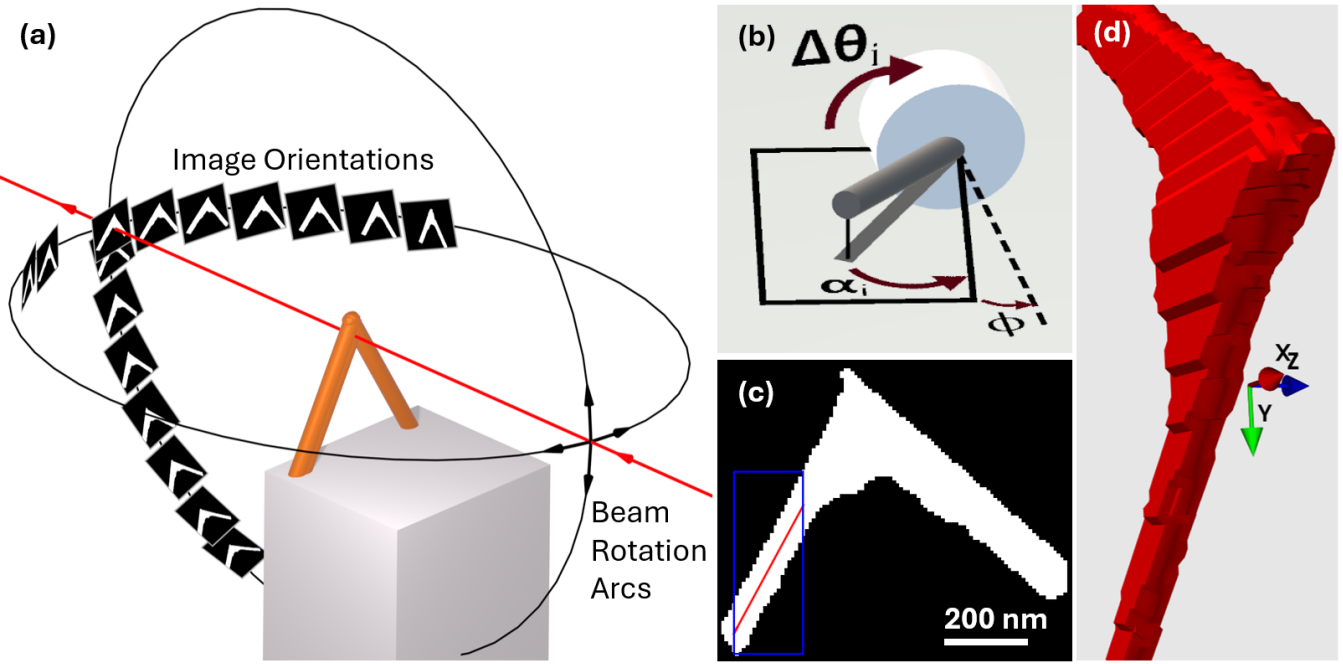


Fig. 5: Tomographic alignment of phase images and generation of the geometric model. (a) Phase image orientations relative to the sample. The diagram shows the angular position and sample outline of every phase image used in the reconstruction. The direction of the electron beam is shown in red, and the arcs of rotation are shown in black. (b) Rotations that define the projections for a conically symmetric element, showing sample tilt $\Delta\theta_i$, projection direction in the detector α_i , and rotation between the detector and tilt-axis ϕ . (c) The centre of an axially symmetric part of the sample can be identified in all projections and is measured to align each projection. (d) CT reconstruction of the masks in the aligned projections. A 10.2 nm voxel size is used to increase computation speed. CT reconstruction is performed to generate a model representing sample geometry and automated alignment is used to improve CT accuracy.

reconstruction volume. The correlation is plotted relative to the $\frac{1}{2}$ bit SNR threshold, commonly used in x-ray tomography [van Heel and Schatz, 2005] and reveals that any feature larger than 14.8 nm has a sufficient SNR to be interpreted directly. The resolution limit of ~ 1.5 pixels due to noise is regarded as conservative since noise is suppressed in regularised reconstructions, hence systematic uncertainties are also considered. The first source of systematic error to consider is the small angle approximation. If the angle between neighbouring atomic spins is larger than 30° , then the micromagnetic energy expressions are no longer valid [Donahue and McMichael, 1997]. The maximum spin angle in Fig. 6b highlights domain walls and shows that calculations are valid for most of the sample, but voxels at the core of the vortex are not resolved.

Other uncertainties can be found with optimal estimation diagnostics [Ungermann et al., 2010] by assuming that all \vec{M} vectors and phase image pixels have probability density functions described by the normal distribution. The reconstructed magnetisation, \vec{M}_{rec} , can be expressed as true \vec{M} transformed by averaging kernel matrix A , which is further changed by measurement errors in phase images, ϵ , according to the error gain matrix G .

$$\vec{M}_{rec} = A\vec{M} + G\epsilon \quad (6)$$

A and G were derived for the \vec{M}_{rec} vector denoted by a star in Fig. 6d that has $\mu_0 M_s = 0.78$ T and is well resolved with a maximum spin angle of 13° . G is used for linear error propagation, because it expresses the error on a single \vec{M}_{rec} vector as a function of error on every pixel in experimental phase measurements. The

phase measurement noise of 0.016 rad per pixel was determined by calculating the standard deviation of vacuum measurements and is mapped by G to a $\mu_0 M_s$ error of 0.001 T. In addition, the experimental and simulated phase images used in the cost function eq. 5 cannot match perfectly due to experimental misalignments, resulting in the residual distribution Fig. 8 corresponding to a root-mean-square error of 0.38 radians. Forcing the reconstruction to match any one image perfectly would, on average, introduce a perturbation that maps to a $\mu_0 M_s$ error of 0.009 T. A is a measure of spatial averaging during the reconstruction and shows that to calculate a single \vec{M}_{rec} vector, information is taken from a volume around the central position, as illustrated in Fig. 9, and for this voxel, the point-spread-function has an average full-width-half-maximum (FWHM) of 43 nm. Evaluation of A is an optimised approach equivalent to changing the value of one voxel of \vec{M}_{rec} and repeating the reconstruction to quantify systematic errors. Error propagation and perturbation mapping for other voxels yields similar results, therefore the $\mu_0 M_s$ measurement precision is determined as 0.01 T per pixel, and the spatial resolution is 50 nm.

For this dataset, it is possible to perform the reconstruction with a voxel size of 5.1 nm instead of 10.2 nm, but smaller voxels are more strongly affected by noise and phase image misalignments, resulting in reduced precision per pixel. During reconstruction, gradient regularisation is necessary to obtain ferromagnetic solutions, but it also suppresses noise, applies smoothing to sharp features, and can be adjusted to vary the trade-off between precision and spatial resolution. If the precision

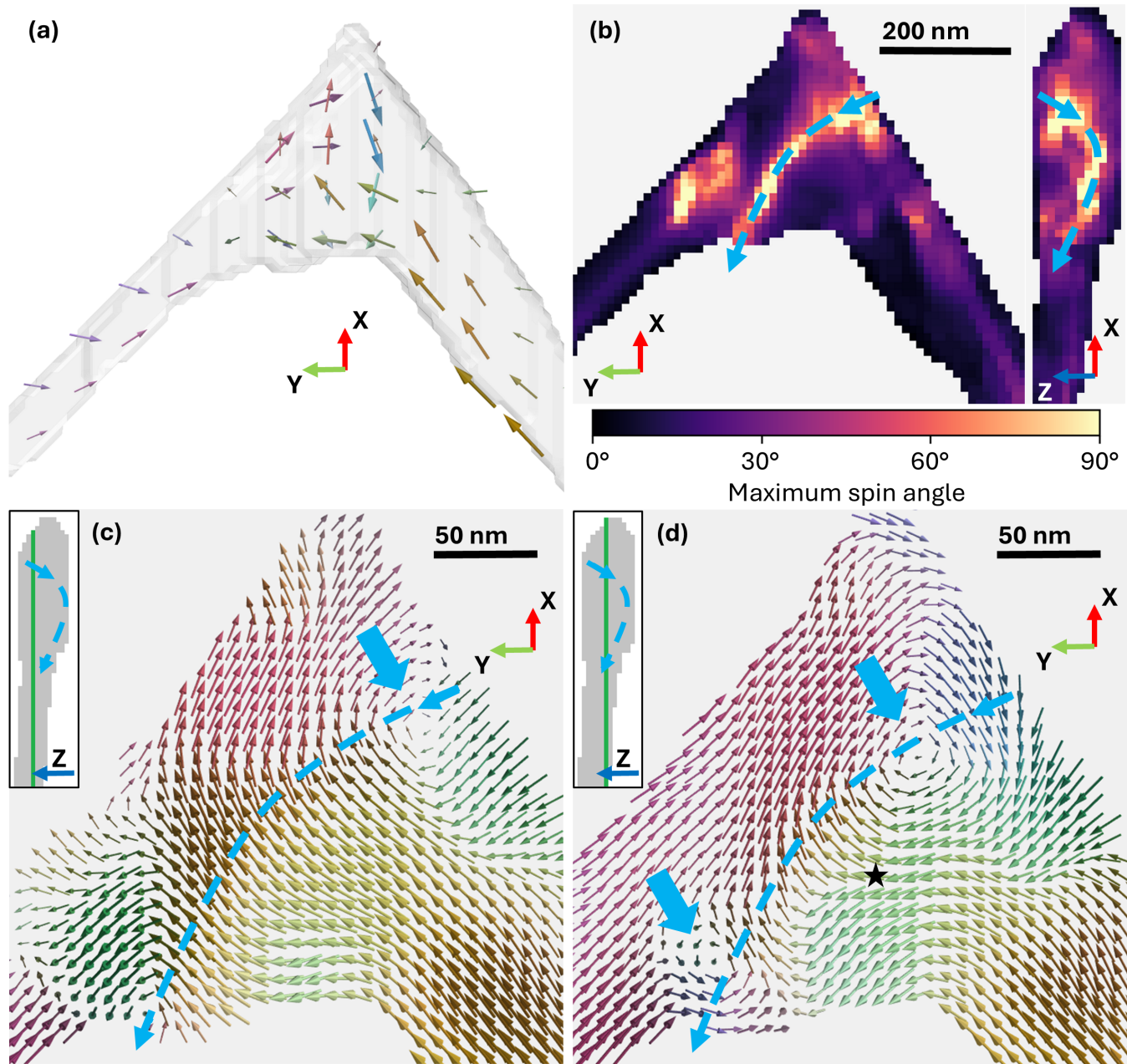


Fig. 6: Reconstructed 3D \bar{M}_{rec} distribution in the FEBID cobalt nanostructure. (a) 3D \bar{M}_{rec} vector field. (b) The maximum angle between neighbouring spins, projected along the z and y axes. The dashed line shows the curve defined by the core of the vortex domain wall. (c), (d) Single-plane slices of the \bar{M}_{rec} vector field shown at full resolution. The insets define the locations of the slices, the vortex state core is marked as in (b), and blue arrows indicate where the slices intersect the vortex core. The vortex core follows a curve where the top slice (c) intersects it once, and the bottom slice (d) intersects twice. The star in (d) denotes a voxel selected for diagnostics of the reconstruction. The reconstruction is a 3D vector field showing the direction and magnitude of magnetic moments inside the sample.

for smaller voxels is increased to 0.01 T by adjusting the regulariser weights, it results in a spatial resolution of 50 nm, showing that the resolution is largely independent of voxel size for voxels smaller than 10 nm. This is attributed to remaining uncorrected phase image misalignments that result in smoothing of features in the reconstruction. Using 10.2 nm voxel size, the MBIR algorithm computes a reconstruction in 3 hours using one core of an Intel i7 central processing unit (CPU). The algorithm optimisations are

discussed in the supplementary material [S4]. Achieving higher resolution would first require advanced image drift correction algorithms to be applied and then for the reconstruction software to be optimised for smaller voxel sizes. Possible implementations are discussed later.

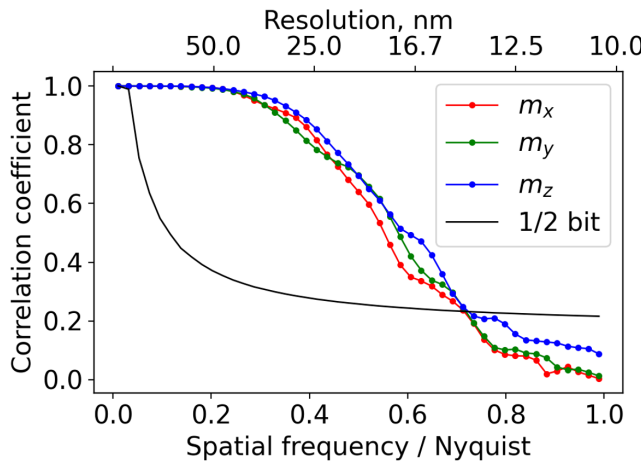


Fig. 7: Fourier shell correlation evaluating the SNR for separate spatial frequency bands. Reconstructed features larger than 14.8 nm have sufficient SNR to be interpreted directly.

Results

Uniform region reconstruction

H-VFET and MBIR have been used to record and reconstruct the 3D \vec{M}_{rec} in a sample consisting of two intersecting nanowires. Fig. 3e shows that FEBID nanowires consist of a mixture of cobalt and organic compounds that transitions from pure carbon shell at the surface up to 60% cobalt content in the core. Since the cobalt is dispersed within the carbon matrix in nanocrystalline form [Pablo-Navarro et al., 2018] and bulk cobalt has $\mu_0 M_s = 1.75$ T [Pablo-Navarro et al., 2018], the nanowires should exhibit $\mu_0 M_s < 1.1$ T as observed for the nanowire distribution in Fig. 10. The few outliers with $\mu_0 M_s > 1.1$ T are attributed as artefacts of digitising the interface between magnetic material and vacuum, where magnetic voxels designated as non-magnetic force the reconstruction to compensate and increase the value of M_s on the surface. In other parts of the sample, there are surface voxels containing non-magnetic material where M_s is close to zero. The surface reconstruction artefacts are present because the missing wedge correction for the geometric model is not perfect, and its effects are discussed further in the supplementary material [S1]. The threshold for creating the 3D geometric model in Fig. 5d is refined after the first reconstruction, such that similar amounts of over- and underestimating surface artefacts are present. Such surface artefacts are also identifiable for the full sample as voxels with $\mu_0 M_s > 1.75$ T in the histogram Fig. 10. These errors could be further reduced by using smaller voxel volume and more sensitive tomographic alignment algorithms. For nanowire core measurements, both nanowires have single magnetic domain configurations at a distance 200 nm from the intersection, and measure $\mu_0 M_s = 0.7 \pm 0.2$ T for the left nanowire and $\mu_0 M_s = 0.5 \pm 0.2$ T for the right. M_s has previously been measured for varying cobalt content of FEBID nanowires [Teresa et al., 2016, Pablo-Navarro et al., 2018] but the measurements were corrected to exclude the non-magnetic shell. The correction is replicated by assuming that the Fig. 3e compositional line profile corresponds to a circular-cross-section nanowire with a 100 nm diameter magnetic core; thus, estimating an average cobalt content of 61% with 4% composition standard deviation, which predicts $\mu_0 M_s = 0.5 \pm 0.1$.

Overall, the reconstructed \vec{M}_{rec} agrees with the predicted values but shows a higher standard deviation due to surface artefacts.

Multi-domain reconstruction

The main advantage of reconstructing the \vec{M}_{rec} is visualising the thickness variation of magnetic domains and identifying twisting DWs. Fig. 6a and Fig. 3c are both projected along the z-axis and the close to anti-parallel \vec{M}_{rec} vectors in Fig. 6a explain the phase shift variations at the projected nanowire intersection in Fig. 3c. Furthermore, the $\text{curl}(\vec{M}_{rec})$ direction in Fig. 6b shows that in Fig. 3c only part of the vortex has curl oriented close to the z-axis and is visible, whilst the other part is more in-plane and required imaging over a second tilt arc for sufficient signal to be detected. Notably, the vortex core is curved to favour positioning at the protrusion at the bottom of the intersection, considered to be a DW pinning site. The 50 nm spatial resolution is evident in Fig. 6c where the indicated vortex core has a lower M_s than surrounding material due to spatial averaging of opposite sign vector components. This averaging is the result of the regularisation in eq. 5, where the preferential selection of solutions with low gradients introduces smoothing. Whilst this is necessary to constrain \vec{M}_{rec} solutions to ferromagnetic ordering, averaging of anti-parallel vectors offsets M_s values at vortex cores. In this experiment, this M_s offset due to spatial averaging is negligible compared to variations in material composition. The elemental map Fig. 3d evaluates the cobalt purity at the intersection as $70 \pm 15\%$ with a predicted $\mu_0 M_s = 0.8 \pm 0.5$ T [Teresa et al., 2016, Pablo-Navarro et al., 2018, Donnelly et al., 2022], and is good agreement with $\mu_0 M_s = 0.9 \pm 0.3$ T measured in the reconstruction. The DW occupies the full ~ 200 nm width volume of the intersection, which is comparable to ~ 100 nm DW width for transverse head-to-head DWs that have previously been observed using magnetic X-ray laminography in 80% purity FEBID cobalt nanowire double helices [Donnelly et al., 2022]. In summary, MBIR has accurately measured M_s for a U-shaped vortex DW of 200 nm width but showed to be less sensitive to sub-50 nm M_s variations, as indicated by lower-than-expected measurement standard deviation.

Discussion

Algorithm improvements

The 3D spatial resolution could be significantly improved by reducing voxel size, as this would reduce the extent of spatial averaging. Since imposing ferromagnetic ordering requires a comparison of neighbouring voxels, the resolution is limited to approximately three times the voxel size, therefore 3 nm 3D resolution would be possible if a voxel size of 1 nm was used. Such resolution improvement would increase the computation time one thousand fold, but existing technology can mitigate the impact. The MBIR algorithm can be parallelised to benefit from computing on dedicated servers, and the conjugate gradient minimisation could be replaced by a linear least squares solver to reduce the number of minimisation steps if the variance regularisation in eq. 5 was removed [Virtanen et al., 2020]. The current symmetry-based tomographic alignment would have to be replaced as it shows up to 10 nm image alignment errors when applied to samples comprised of more than a single cylindrical nanowire, where more general algorithms would be suitable [Penczek et al., 1996, Houben and Bar Sadan, 2011]. Finally, electron holography can measure phase with sub-nm spatial resolution by reducing interference

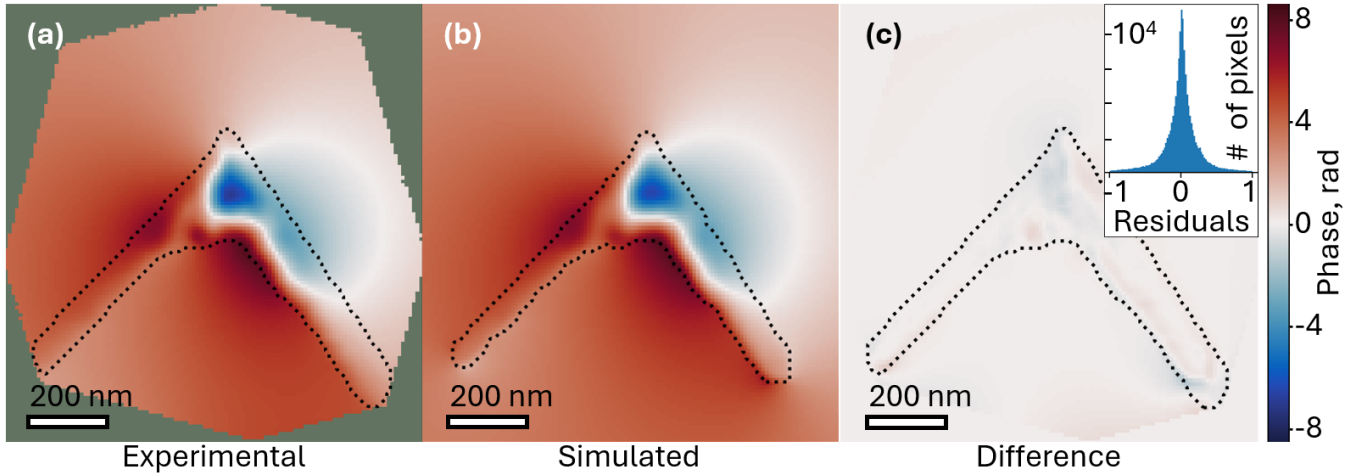


Fig. 8: Magnetic phase shift reconstruction for the phase image at -3.7° tilt. (a) Experimental phase image. (b) Reconstructed phase image. (c) Difference between (a) and (b). The inset shows the combined distribution of residual differences for phase images at all tilt angles. The phase image residuals are propagated to estimate \vec{M}_{rec} reconstruction uncertainty.

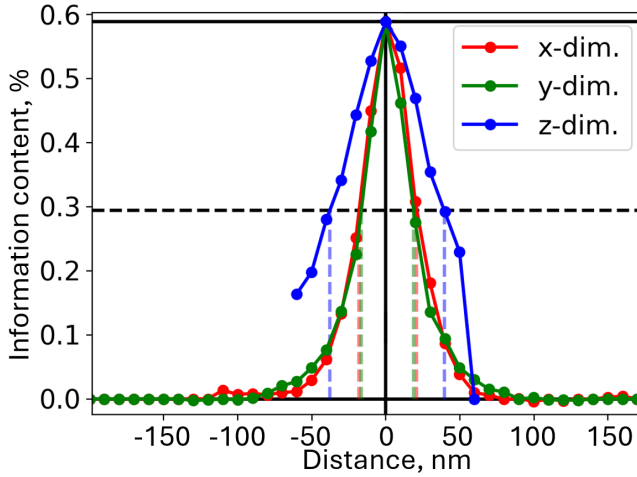


Fig. 9: 3D point-spread function. Spatial distribution of information content for the voxel denoted by a star in Fig. 6d. During the reconstruction, information contained at this point in space is spread over a volume with an average FWHM of 43 nm.

fringe spacing [Dunin-Borkowski et al., 2019] and can be used to acquire high-resolution tomographic datasets. Once the software is optimised for supercomputer use, it can also be applied for \vec{M} reconstruction of atomic resolution electron holography [Tanigaki et al., 2024].

Outlook

This study shows a quantitative reconstruction of 3D \vec{M} for a cobalt FEBID nanostructure using H-VFET. Commonly, H-VFET datasets are used to reconstruct \vec{B} in 3D [Prabhat et al., 2017, Wolf et al., 2019, Lewis et al., 2023] but they may also be used to reconstruct \vec{M} subject to limitations outlined in this paper. 3D \vec{M} reconstructions were tested with a range of FEBID nanowires of varying purity and the FEBID nanowire intersection is presented as it combines the complexity arising from the non-uniformity of

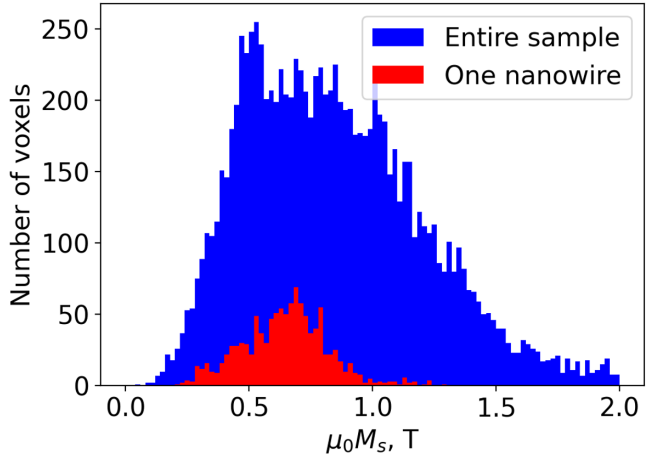


Fig. 10: Distribution of \vec{M}_{rec} magnitudes. All voxels in the sample are shown in blue, and the voxels in the nanowire on the left side of Fig. 6a are shown in red. Bin size is 0.02 T. The distribution shows known material composition variations and some reconstruction artefacts.

the material with the possibility of projection-based null spaces from a 3D vortex DW. The result is an accurate reconstruction that requires 16 projections with 10° angular spacing over two tilt-axes to achieve 50 nm spatial resolution. For other nanostructures, by comparison of these experimental results and simulations, reconstruction of \vec{M} is considered possible if all the following conditions are met:

- Sample geometry must be defined. Errors arising from an inaccurate geometric model are discussed in supplementary material [S1].
- Phase shift arising from all components of \vec{M} must be measured. In general, two complete tilt arcs are necessary, but in the case of uniform nanowires and vortex states, lower tilt

ranges are viable but increase reconstruction error as discussed in supplementary material [S1].

- There must not be external magnetic fields, nor conduction or displacement currents in the sample. This ensures that all measured phase shifts are due to \vec{M} .
- The sample must be ferromagnetic. This is a requirement for the MBIR algorithm.

In addition, if null spaces are present, they only affect the adjacent sub-volume, as discussed in supplementary material [S2], and other sub-volumes of the reconstruction are quantitative. The ferromagnetic nanostructure shown in this paper satisfies the above conditions because the sample dimensions have been measured during fabrication and were applied to correct the missing wedge in the generated geometric model; \vec{M} configurations present in the sample do not create null spaces and can, theoretically, be reconstructed with less than 1% error when imaged over $\pm 60^\circ$ tilt arcs; and the sample is isolated from other materials that may accumulate change or be magnetised.

Previous works have shown 2D reconstructions of \vec{M} [Kovács et al., 2017, Song et al., 2018], and an alternative MBIR implementation [Mohan et al., 2018] with only qualitative 3D reconstruction. In comparison, micromagnetic simulations [Wolf et al., 2022, Lyu et al., 2024] are a common approach to 3D quantification, but require knowledge of the material magnetic properties, whereas MBIR can, in special cases, reconstruct \vec{M} without prior knowledge. Regarding other probes, quantitative measurements have been shown using both X-ray and neutron tomography [Donnelly et al., 2017, Hilger et al., 2018, Donnelly et al., 2020, 2022, Di Pietro Martínez et al., 2023] with the best \vec{M} spatial resolution of 50 nm for X-ray laminography, which is comparable to MBIR. With improved spatial resolution MBIR would be uniquely suited to characterise 3D magnetic nanostructures, such as nanowire junctions, interfaces in nanoparticles, Bloch-type skyrmions on curved surfaces, and hopfions.

Conclusions

An electron microscopy method has been developed to image multiple projections of electromagnetic fields from a ferromagnetic nanostructure and reconstruct a possible corresponding 3D \vec{M} distribution, subject to considerations of null space limitations. This experiment shows that MBIR can be applied to reconstruct \vec{M} from a H-VFET dataset, if a magnetic TEM signal is detected from all parts of the sample, and image matching & tomographic alignment routines are applied to correct the experimental dataset. Optimal estimation diagnostics show that reconstruction has 0.01 T precision at each voxel and a spatial resolution of 50 nm, which can be greatly improved by optimising the computation to allow smaller voxel size and correcting tomographic misalignments with higher precision.

Availability of Data and Materials

Data is available on request. Software and example datasets are available from repositories listed in supplementary materials [S3].

Acknowledgements

The authors acknowledge Patrick Diehle for the experimental development of H-VFET, Jan Caron for the theoretical development of \vec{M} reconstruction with MBIR, and the Helmholtz fellowship.

Funding

The authors are grateful for funding from the Engineering and Physical Science Research Council (Grant No. EP/W524359/1 and EP/X025632/1), European Research Council under the European Union's Horizon 2020 Research and Innovation Programme (Grant No. 856538, project "3D MAGiC") and to the Deutsche Forschungsgemeinschaft (Project-ID 405553726 TRR270).

Conflict of interest

The authors declare none.

Author contributions

AS: Software, Formal analysis, Writing – original draft. AK: Supervision, Methodology, Writing – review & editing. SMV: Writing – review & editing. REDB: Writing – review & editing. KF: Writing – review & editing. TPA: Supervision, Methodology, Writing – review & editing.

References

Fengshan Zheng, Nikolai S. Kiselev, Philipp N. Rybakov, Luyan Yang, Wen Shi, Stefan Blügel, and Rafal E. Dunin-Borkowski. Hopfion rings in a cubic chiral magnet. *Nature*, 623(7988):718–723, 2023.

Stuart S. P. Parkin, Masamitsu Hayashi, and Luc Thomas. Magnetic Domain-Wall Racetrack Memory. *Science*, 320(5873):190–194, 2008.

Matthew O. A. Ellis, Alexander Welbourne, Stephan J. Kyle, Paul W. Fry, Dan A. Allwood, Thomas J. Hayward, and Eleni Vasilaki. Machine learning using magnetic stochastic synapses. *Neuromorph. Comput. Eng.*, 3(2):021001, 2023.

Dmitri E. Nikonov, George I. Bourianoff, and Paolo A. Gargini. Power Dissipation in Spintronic Devices Out of Thermodynamic Equilibrium. *J Supercond*, 19(6):497–513, 2006.

Ke Gu, Yicheng Guan, Binoy Krishna Hazra, Hakan Deniz, Andrea Migliorini, Wenjie Zhang, and Stuart S. P. Parkin. Three-dimensional racetrack memory devices designed from freestanding magnetic heterostructures. *Nat. Nanotechnol.*, 17(10):1065–1071, 2022.

Claire Donnelly, Simone Finizio, Sebastian Gliga, Mirko Holler, Aleš Hrabec, Michal Odstrčil, Sina Mayr, Valerio Scagnoli, Laura J. Heyderman, Manuel Guizar-Sicairos, and Jörg Raabe. Time-resolved imaging of three-dimensional nanoscale magnetization dynamics. *Nat. Nanotechnol.*, 15(5):356–360, 2020.

Claire Donnelly, Manuel Guizar-Sicairos, Valerio Scagnoli, Sebastian Gliga, Mirko Holler, Jörg Raabe, and Laura J. Heyderman. Three-dimensional magnetization structures revealed with X-ray vector nanotomography. *Nature*, 547(7663):328–331, 2017.

Marisel Di Pietro Martínez, Alexis Wartelle, Carlos Herrero Martínez, Farid Fettar, Florent Blondelle, Jean-François Motte, Claire Donnelly, Luke Turnbull, Feodor Ogrin, Gerrit van der Laan, Horia Popescu, Nicolas Jaouen, Flora Yakhou-Harris, and Guillaume Beutier. Three-dimensional tomographic imaging of the magnetization vector field using Fourier transform holography. *Phys. Rev. B*, 107(9):094425, 2023.

Claire Donnelly, Aurelio Hierro-Rodríguez, Claas Abert, Katharina Witte, Luka Skoric, Dédalo Sanz-Hernández, Simone Finizio, Fanfan Meng, Stephen McVitie, Jörg Raabe, Dieter Suess, Russell Cowburn, and Amalio Fernández-Pacheco. Complex free-space magnetic field textures induced by three-dimensional magnetic nanostructures. *Nat. Nanotechnol.*, 17(2):136–142, 2022.

C. Phatak, M. Beleggia, and M. De Graef. Vector field electron tomography of magnetic materials: Theoretical development. *Ultramicroscopy*, 108(6):503–513, 2008.

Charudatta Phatak, Amanda K. Petford-Long, and Marc De Graef. Three-Dimensional Study of the Vector Potential of Magnetic Structures. *Phys. Rev. Lett.*, 104(25):253901, 2010.

Daniel Wolf, Nicolas Biziere, Sebastian Sturm, David Reyes, Travis Wade, Tore Niermann, Jonas Krehl, Benedicte Warot-Fonrose, Bernd Büchner, Etienne Snoeck, Christophe Gatel, and Axel Lubk. Holographic vector field electron tomography of three-dimensional nanomagnets. *Commun Phys.*, 2(1):1–9, 2019.

M. J. Donahue and R. D. McMichael. Exchange energy representations in computational micromagnetics. *Physica B: Condensed Matter*, 233(4):272–278, 1997.

Boya Lyu, Shihua Zhao, Yibo Zhang, Weiwei Wang, Fengshan Zheng, Rafal E. Dunin-Borkowski, Jiadong Zang, and Haifeng Du. Three-dimensional magnetization reconstruction from electron optical phase images with physical constraints. *Sci. China Phys. Mech. Astron.*, 67(11):117511, 2024.

Jan Caron. *Model-based reconstruction of magnetisation distributions in nanostructures from electron optical phase images*. PhD thesis. Forschungszentrum Jülich GmbH Zentralbibliothek, Verlag, Jülich, 2018a.

A. Lubk and J. Zweck. Differential phase contrast: An integral perspective. *Phys. Rev. A*, 91(2):023805, 2015.

Amit Kohn, Avihay Habibi, and Martin Mayo. Experimental evaluation of the ‘transport-of-intensity’ equation for magnetic phase reconstruction in Lorentz transmission electron microscopy. *Ultramicroscopy*, 160:44–56, 2016.

Matus Krajanek, Damien McGrouther, Dzmitry Maneuski, Val O’ Shea, and Stephen McVitie. Pixelated detectors and improved efficiency for magnetic imaging in STEM differential phase contrast. *Ultramicroscopy*, 165:42–50, 2016.

Shengbo You, Peng-Han Lu, Thomas Schachinger, András Kovács, Rafal E. Dunin-Borkowski, and Andrew M. Maiden. Lorentz near-field electron ptychography. *Applied Physics Letters*, 123(19):192406, 2023.

Jizhe Cui, Haozhi Sha, Wenfeng Yang, and Rong Yu. Antiferromagnetic imaging via ptychographic phase retrieval. *Science Bulletin*, 69(4):466–472, 2024.

Y. Aharonov and D. Bohm. Significance of Electromagnetic Potentials in the Quantum Theory. *Phys. Rev.*, 115(3):485–491, 1959.

S. McVitie and G. S. White. Imaging Amperian currents by Lorentz microscopy. *J. Phys. D: Appl. Phys.*, 37(2):280, 2003.

F. Junginger, M. Kläui, D. Backes, S. Krzyk, U. Rüdiger, T. Kasama, R. E. Dunin-Borkowski, J.-M. Feinberg, R. J. Harrison, and L. J. Heyderman. Quantitative determination of vortex core dimensions in head-to-head domain walls using off-axis electron holography. *Applied Physics Letters*, 92(11):112502, 2008.

K. Aditya Mohan, Prabhat KC, Charudatta Phatak, Marc De Graef, and Charles A. Bouman. Model-Based Iterative Reconstruction of Magnetization Using Vector Field Electron Tomography. *IEEE Transactions on Computational Imaging*, 4(3):432–446, 2018.

L. Houben and M. Bar Sadan. Refinement procedure for the image alignment in high-resolution electron tomography. *Ultramicroscopy*, 111(9):1512–1520, 2011.

Jan Caron. Magnetisation reconstruction in three dimensions. In *Model-based reconstruction of magnetisation distributions in nanostructures from electron optical phase images*, pages 119–140. PhD thesis. Forschungszentrum Jülich GmbH Zentralbibliothek, Verlag, Jülich, 2018b.

Patrick Diehle, András Kovács, Thomas Duden, Rolf Speen, Kristina Žagar Soderžnik, and Rafal E. Dunin-Borkowski. A cartridge-based turning specimen holder with wireless tilt angle measurement for magnetic induction mapping in the transmission electron microscope. *Ultramicroscopy*, 220:113098, 2021.

M. Mansuripur. Computation of electron diffraction patterns in Lorentz electron microscopy of thin magnetic films. *Journal of Applied Physics*, 69(4):2455–2464, 1991.

Jan Caron. Reconstructibility and null spaces. In *Model-based reconstruction of magnetisation distributions in nanostructures from electron optical phase images*, pages 74–82. PhD thesis. Forschungszentrum Jülich GmbH Zentralbibliothek, Verlag, Jülich, 2018c.

Luka Skoric, Dédalo Sanz-Hernández, Fanfan Meng, Claire Donnelly, Sara Merino-Aceituno, and Amalio Fernández-Pacheco. Layer-by-Layer Growth of Complex-Shaped Three-Dimensional Nanostructures with Focused Electron Beams. *Nano Lett.*, 20(1):184–191, 2020.

César Magén, Javier Pablo-Navarro, and José María De Teresa. Focused-Electron-Beam Engineering of 3D Magnetic Nanowires. *Nanomaterials*, 11(2):402, 2021.

Luis Serrano-Ramón, Rosa Córdoba, Luis Alfredo Rodríguez, César Magén, Etienne Snoeck, Christophe Gatel, Inés Serrano, Manuel Ricardo Ibarra, and José María De Teresa. Ultrasmall Functional Ferromagnetic Nanostructures Grown by Focused Electron-Beam-Induced Deposition. *ACS Nano*, 5(10):7781–7787, 2011.

Rafal E. Dunin-Borkowski, András Kovács, Takeshi Kasama, Martha R. McCartney, and David J. Smith. Electron Holography. In Peter W. Hawkes and John C. H. Spence, editors, *Springer Handbook of Microscopy*, pages 767–818. Springer International Publishing, Cham, 2019.

D. R. G. Mitchell and B. Schaffer. Scripting-customised microscopy tools for Digital Micrograph™. *Ultramicroscopy*, 103(4):319–332, 2005.

Victor Boureau, Robert McLeod, Benjamin Mayall, and David Cooper. Off-axis electron holography combining summation of hologram series with double-exposure phase-shifting: Theory and application. *Ultramicroscopy*, 193:52–63, 2018.

Matthew Weyland and Paul Midgley. Electron Tomography. In C. Barry Carter and David B. Williams, editors, *Transmission*

Electron Microscopy: Diffraction, Imaging, and Spectrometry, pages 343–376. Springer International Publishing, Cham, 2016.

Stéfan van der Walt, Johannes L. Schönberger, Juan Nunez-Iglesias, François Boulogne, Joshua D. Warner, Neil Yager, Emmanuelle Gouillart, and Tony Yu. scikit-image: image processing in Python. *PeerJ*, 2:e453, 2014.

Francisco de la Peña, Eric Prestat, Vidar Tonaas Fauske, Pierre Burdet, Petras Jokubauskas, Magnus Nord, Tomas Ostasevicius, Katherine E. MacArthur, Mike Sarahan, Duncan N. Johnstone, Joshua Taillon, Jonas Lähnemann, Vadim Migunov, Alberto Eljarrat, Jan Caron, Thomas Aarholt, Stefano Mazzucco, Michael Walls, Tom Slater, Florian Winkler, pquinn dls, Ben Martineau, Gaël Donval, Robert McLeod, Eric R. Hoglund, Ivo Alxneit, Daniel Lundeby, Trond Henninen, Luiz Fernando Zagonel, and Andreas Garmannslund. hyperspy/hyperspy: HyperSpy v1.5.2, 2019.

Gary W Paterson, Robert W H Webster, Andrew Ross, Kirsty A Paton, Thomas A Macgregor, Damien McGrouther, Ian MacLaren, and Magnus Nord. Fast Pixelated Detectors in Scanning Transmission Electron Microscopy. Part II: Post-Acquisition Data Processing, Visualization, and Structural Characterization. *Microscopy and Microanalysis*, 26(5):944–963, 2020.

Pawel A. Penczek, Jun Zhu, and Joachim Frank. A common-lines based method for determining orientations for $N > 3$ particle projections simultaneously. *Ultramicroscopy*, 63(3):205–218, 1996.

Pauli Virtanen, Ralf Gommers, Travis E. Oliphant, Matt Haberland, Tyler Reddy, David Cournapeau, Evgeni Burovski, Pearu Peterson, Warren Weckesser, Jonathan Bright, Stéfan J. van der Walt, Matthew Brett, Joshua Wilson, K. Jarrod Millman, Nikolay Mayorov, Andrew R. J. Nelson, Eric Jones, Robert Kern, Eric Larson, C. J. Carey, İlhan Polat, Yu Feng, Eric W. Moore, Jake VanderPlas, Denis Laxalde, Josef Perktold, Robert Cimrman, Ian Henriksen, E. A. Quintero, Charles R. Harris, Anne M. Archibald, Antônio H. Ribeiro, Fabian Pedregosa, and Paul van Mulbregt. SciPy 1.0: fundamental algorithms for scientific computing in Python. *Nat Methods*, 17(3):261–272, 2020.

Jan Caron. A forward model for the calculation of the magnetic phase. In *Model-based reconstruction of magnetisation distributions in nanostructures from electron optical phase images*, pages 21–57. PhD thesis. Forschungszentrum Jülich GmbH Zentralbibliothek, Verlag, Jülich, 2018d.

Jorge Nocedal and Stephen J. Wright, editors. *Numerical Optimization*. Springer New York, 2006.

Marin van Heel and Michael Schatz. Fourier shell correlation threshold criteria. *Journal of Structural Biology*, 151(3):250–262, 2005.

J. Ungermaann, M. Kaufmann, L. Hoffmann, P. Preusse, H. Oelhaf, F. Friedl-Vallon, and M. Riese. Towards a 3-D tomographic retrieval for the air-borne limb-imager GLORIA. *Atmospheric Measurement Techniques*, 3(6):1647–1665, 2010.

Javier Pablo-Navarro, César Magén, and José María de Teresa. Purified and Crystalline Three-Dimensional Electron-Beam-Induced Deposits: The Successful Case of Cobalt for High-Performance Magnetic Nanowires. *ACS Appl. Nano Mater.*, 1(1):38–46, 2018.

J. M. De Teresa, A. Fernández-Pacheco, R. Córdoba, L. Serrano-Ramón, S. Sangiao, and M. R. Ibarra. Review of magnetic nanostructures grown by focused electron beam induced deposition (FEBID). *J. Phys. D: Appl. Phys.*, 49(24):243003, 2016.

Toshiaki Tanigaki, Tetsuya Akashi, Takaho Yoshida, Ken Harada, Kazuo Ishizuka, Masahiko Ichimura, Kazutaka Mitsuishi, Yasuhide Tomioka, Xiuzhen Yu, Daisuke Shindo, Yoshinori Tokura, Yasukazu Murakami, and Hiroyuki Shinada. Electron holography observation of individual ferrimagnetic lattice planes. *Nature*, 631(8021):521–525, 2024.

K. C. Prabhat, K. Aditya Mohan, Charudatta Phatak, Charles Bouman, and Marc De Graef. 3D reconstruction of the magnetic vector potential using model based iterative reconstruction. *Ultramicroscopy*, 182:131–144, 2017.

George R. Lewis, Daniel Wolf, Axel Lubk, Emilie Ringe, and Paul A. Midgley. WRAP: A wavelet-regularised reconstruction algorithm for magnetic vector electron tomography. *Ultramicroscopy*, 253:113804, 2023.

András Kovács, Jan Caron, Andrii S. Savchenko, Nikolai S. Kiselev, Kiyou Shibata, Zi-An Li, Naoya Kanazawa, Yoshinori Tokura, Stefan Blügel, and Rafal E. Dunin-Borkowski. Mapping the magnetization fine structure of a lattice of Bloch-type skyrmions in an FeGe thin film. *Applied Physics Letters*, 111(19):192410, 2017.

Dongsheng Song, Zi-An Li, Jan Caron, András Kovács, Huanfang Tian, Chiming Jin, Haifeng Du, Mingliang Tian, Jianqi Li, Jing Zhu, and Rafal E. Dunin-Borkowski. Quantification of Magnetic Surface and Edge States in an FeGe Nanostripe by Off-Axis Electron Holography. *Phys. Rev. Lett.*, 120(16):167204, 2018.

Daniel Wolf, Sebastian Schneider, Ulrich K. Rößler, András Kovács, Marcus Schmidt, Rafal E. Dunin-Borkowski, Bernd Büchner, Bernd Rellinghaus, and Axel Lubk. Unveiling the three-dimensional magnetic texture of skyrmion tubes. *Nat. Nanotechnol.*, 17(3):250–255, 2022.

A. Hilger, I. Manke, N. Kardjilov, M. Osenberg, H. Markötter, and J. Banhart. Tensorial neutron tomography of three-dimensional magnetic vector fields in bulk materials. *Nat Commun*, 9(1):4023, 2018.